Journal of Hydrology 612 (2022) 128028

Contents lists available at ScienceDirect

Journal of Hydrology

journal homepage: www.elsevier.com/locate/jhydrol

Technical Note

A multiscale finite element method for coupled heat and water transfer in heterogeneous soils

Chenyi Luo [a], Yuanyuan Shi [b,*], Dennis Timlin [c], Robert Ewing [d], David Fleisher [c], Robert Horton [e], Katherine Tully [f], Zhuangji Wang [c,f,*]

[a] School of Life Sciences, Beijing University of Chinese Medicine, Beijing 102488, China
[b] Shenzhen Research Institute, Beijing University of Chinese Medicine, Shenzhen 518118, China
[c] Adaptive Cropping System Laboratory, USDA-ARS, Beltsville, MD 20705, USA
[d] The Climate Corporation, 710 2nd Ave., Suite 1100, Seattle, WA 98104, USA
[e] Department of Agronomy, Iowa State University, Ames, IA 50011, USA
[f] Department of Plant Science and Landscape Architecture, University of Maryland, College Park, MD 20742, USA

ARTICLE INFO

This manuscript was handled by Jiri Simunek, Editor-in-Chief, with the assistance of Giuseppe Brunetti, Associate Editor

Keywords:
Coupled heat and water transfer (CHWT)
Multiscale finite element method (MsFEM)
Numerical simulation

ABSTRACT

Large-scale modeling of coupled heat and water transfer (CHWT) is challenging due to the spatial variabilities of soil hydraulic and thermal properties. A multi-scale finite element method (MsFEM) has been designed for simulating liquid water fluxes in unsaturated soils. In this study, the MsFEM approach is expanded as a new scheme that can handle CHWT in soils. Two groups of MsFEM basis functions are constructed to incorporate the heterogeneities in soil hydraulic conductivity and thermal conductivity, and a Petrov-Galerkin formulation is adopted to implement the proposed MsFEM scheme. The MsFEM scheme is also exploited as a sequential solver when heat transfer and water transfer are expressed in a partially coupled formulation (Wang et al., 2022a). Numerical examples illustrate that, without essentially increasing the computing load, the MsFEM scheme can improve the accuracy by up-to 30% compared to the standard finite element method (FEM), especially for thermally driven water transfer. Some fine scale spatial variations in soil temperature can only be revealed with the MsFEM scheme. If the MsFEM sequential solver is applied, the coupled heat and water transfer model can be rewritten into a sequence of modules, where liquid water transfer, heat transfer and vapor transfer are solved step-by-step, but the thermally driven liquid water is omitted due to its relatively small value (Wang et al., 2022a). With the MsFEM sequential solver, a flexible modeling architecture can be achieved at the cost of a relatively small increase of error (<5%). Therefore, the MsFEM scheme presented in this study is an effective numerical approach to simulating CHWT in heterogeneous soils.

1. Introduction

Simulation of soil heat and water dynamics is important in agricultural and environmental science, especially in arid and semiarid regions, where heat transfer and water transfer are coupled and water transfer occurs in both liquid and vapor phases (Scanlon and Milly, 1994; Zeng et al., 2011a,b). Besides the nonlinearity in the coupled heat and water transfer (CHWT) governing models, spatial heterogeneity in soil hydraulic and thermal properties becomes another challenge to numerical simulations, especially when the study area is relatively large (Rienzner and Gandolfi, 2014; Shangguan et al., 2014) and when the soil is treated nonuniformly (e.g., local compaction or consolidation in Li et al., 2021; Wang et al., 2022b or uneven soil water content and solute distributions in Wang et al., 2017a; Wang et al., 2021a). When the finite element method (standard FEM, hereafter) is used, relatively fine spatial grids have to be adopted to elucidate the small-scale soil variabilities and to accurately predict the spatial distributions of soil water content and temperature. Refining the spatial grid will tremendously increase the computing load, execution time and the quantity of small-scale soil water and temperature data, which could be unnecessarily detailed for large-scale, regional soil management practices. However, using coarse grids may misrepresent soil heterogeneity and reduce the simulation accuracy, even for large-scale spatial domains. Therefore, a multiscale numerical method that can map small-scale soil properties onto coarse

* Corresponding authors at: Adaptive Cropping System Laboratory, USDA-ARS, Beltsville, MD 20705, USA.
E-mail addresses: yshi@bucm.edu.cn (Y. Shi), zhuangji.wang@usda.gov, cauwzj@gmail.com (Z. Wang).

https://doi.org/10.1016/j.jhydrol.2022.128028
Received 29 January 2022; Received in revised form 23 May 2022; Accepted 3 June 2022
Available online 7 July 2022

grids and perform soil CHWT simulations on the coarse grids up to a required accuracy level is needed.

The multiscale finite element method (MsFEM) is a "fine-to-coarse" numerical approach (Efendiev and Hou, 2009). MsFEM is based on the multiscale variational method, originally reported by Babuska and Osborn (1983), and then developed by Hou and Wu (1997) and Hou et al. (1999) for fluid mechanics in porous media. In fine grids, a series of localized, numerical MsFEM basis functions are chosen to incorporate the small-scale soil features. In coarse grids, the MsFEM basis functions, rather than polynomial basis functions in standard FEM, are used to establish a discretized numerical scheme, which is also referred to as the "global formulation". By doing that, the small-scale soil heterogeneities in the fine grid are first absorbed by the MsFEM basis functions and then transferred to the global formulation in the coarse grid, which is to say "fine-to-coarse". Basis functions and global formulations are two critical ingredients of MsFEM. From one aspect, MsFEM shares similarities with other multi-scale models with respect to those two ingredients, such as the upscaling-homogenization method, variational multiscale approach, heterogeneous multiscale method and multiscale enrichment method (Durlofsky, 1991; Li et al., 2016; Arbogast and Boyd, 2006; E et al., 2005; Fish and Yuan, 2007). From another aspect, development and applications of MsFEM, especially for soil liquid water transfer, rely on modifications and improvements of the basis functions and the global formulations.

From the perspective of MsFEM basis functions, the boundary values of each basis function relate to the accuracy of the global solution. He and Ren (2006) applied and tested the oscillatory boundary conditions and the oversampling techniques proposed by Hou and Wu (1997) to construct basis functions. Since soil hydraulic conductivity may involve both spatial and temporal variations due to changes in soil water content, He and Ren (2009) adaptively updated the MsFEM basis functions during soil water transfer simulations. Moreover, Spiridonov et al. (2020) applied multiscale methods to construct 2D and 3D basis functions for unstructured fine grids to enable the FEM and discrete fracture approach in complex geometries. Additional endeavors to capture small-scale features include multiscale mapping and the limited use of global information (Efendiev et al. 2004; Aarnes et al., 2008). However, related techniques have not been applied in soil water transfer models yet.

From the perspective of the global formulations, Galerkin and multiscale finite volume methods have been reported in He and Ren (2005; 2006). If global information is adopted, a mixed FEM is usually taken as the global formulation to ensure both local and global conservation of mass or energy. In order to implement MsFEM for nonlinear soil water transfer problems, some linearization should be incorporated to the global formulation, and a commonly used scheme is the relaxation presented by Slodicka (2002) and used in He and Ren (2006). Other types of multiscale methods exist. However, they may not belong to MsFEM in the narrow sense. For example, Chen and Ren (2008) proposed a finite difference heterogeneous multiscale method for soil water transfer modeling. Although the origin of such an algorithm is from the homogenization theory, it includes procedures that transfer small-scale properties from local representative volumes to the global formulations.

MsFEM has been used for unsaturated soil water transfer. However, it has not been fully developed for CHWT problems, especially for the thermally driven water fluxes in relatively dry soils. Despite the two-phase water fluxes and the nonlinearity embedded in the governing models, one difficulty in applying MsFEM is that the hydraulic conductivity and the thermal conductivity may not share the same spatial variations (e.g., Li et al., 2019). Although MsFEM approaches in two-phase immiscible or miscible flows have been proposed for reservoir models (see Section 2.10 in Efendiev and Hou, 2009; Juanes and Patzek, 2010), in those cases, the spatial heterogeneities can be simplified and represented by the flow in one phase using auxiliary parameters, such as "mobility", "saturation" and "water/oil-cut". However, for CHWT problems, two spatial variations in hydraulic and thermal conductivity cannot be simplified as they are in the reservoir models, and they must be handled separately.

Thus, the objectives of this study are to develop a MsFEM scheme that can account for spatial variations of soil properties in both heat transfer and water transfer, apply the MsFEM scheme to CHWT simulations, and present illustrative numerical examples.

2. A MsFEM scheme for coupled heat and water transfer model

In Section 2.1, we review a CHWT model [i.e., the Philip and de Vries (1957) model] and include the spatial heterogeneities of soil hydraulic conductivity and soil thermal conductivity into a set of governing equations. The spatial variability of soil properties is usually expressed via a random field with a pre-specified marginal distribution and spatial correlation functions, which is introduced in Section 2.2. In Section 2.3, we establish a MsFEM scheme for the CHWT model. Illustrative examples with result comparisons and error analyses among a range of grid sizes are provided in Section 2.4. Therefore, Sections 2.1 and 2.2 can be treated as the problem statement, and Sections 2.3 and 2.4 can be treated as the solution.

2.1. Review of the coupled water and heat transfer model

When soil is relatively dry, vapor transfer driven by temperature gradients, rather than liquid water or vapor fluxes under water potential gradients, becomes the dominant means for soil water flux, due to the relatively large temperature gradients and high air-filled porosity. When vapor transfer governs the soil water redistribution, it also contributes to sensible and latent heat fluxes. Hence, in such cases, the heat and water transfer in soil is fully coupled and can be expressed by the following Philip and de Vries (1957) model.

$$\begin{cases} \textit{Water equation}: \; c_{\theta\theta}\dfrac{\partial h}{\partial t} + c_{\theta T}\dfrac{\partial T}{\partial t} = \nabla\cdot\left[\underbrace{d_{mv}(h,T)\nabla h + d_{tv}(h,T)\nabla T}_{\equiv -q_v(h,T)} + \underbrace{k(h,T)\nabla h + d_{tl}(h,T)\nabla T}_{\equiv -q_l(h,T)}\right] & (1a) \\ \textit{Heat equation}: \; c_{T\theta}\dfrac{\partial h}{\partial t} + c_{TT}\dfrac{\partial T}{\partial t} = -\nabla\cdot\left[\underbrace{-\lambda\nabla T + c_l\rho_l q_l(T-T_0) + [L_0\rho_l q_v + c_v\rho_l q_v(T-T_0)\,]}_{=q_h(h,T)}\right] & (1b) \end{cases}$$

In Eq. (1), $c_{\theta\theta}(\mathrm{cm}^{-1})$, $c_{\theta T}(\mathrm{K}^{-1})$, $c_{T\theta}(\mathrm{J\,cm^{-3}\,cm^{-1}})$ and $c_{TT}(\mathrm{J\,cm^{-3}\,K^{-1}})$ are capacity terms related to changes in soil water potential [h, cm, or changes in soil water content $(\theta, \mathrm{cm^3\,cm^{-3}})$ equivalently], and soil temperature (T, K). ∇ indicates the differential operator in a spatial domain Ω. In Eq. (1a), $d_{mv}(h,T)(\mathrm{cm\,s^{-1}})$ and $d_{tv}(h,T)(\mathrm{cm^2\,s^{-1}\,K^{-1}})$ represent vapor diffusivities under the water potential gradient and temperature gradient, respectively. Hence, $q_v(\mathrm{cm\,s^{-1}})$ is the net vapor

flux. Similarly, $k(h,T)\left(\mathrm{cm\,s^{-1}}\right)$ is the (unsaturated) hydraulic conductivity and $d_{tl}(h,T)\left(\mathrm{cm^2\,s^{-1}\,K^{-1}}\right)$ is the coefficient for thermally driven liquid water diffusion. Hence, $q_l(h,T)$ represents the net liquid water flux. In Eq. (1b), $\lambda\left(\mathrm{W\,cm^{-1}\,K^{-1}}\right)$ is the soil thermal conductivity; $L_0\left(\mathrm{J\,g^{-1}}\right)$ is the heat of vaporization of water at a pre-specified reference temperature $T_0(\mathrm{K})$; $c_l \approx 4.187\mathrm{J\,g^{-1}\,K^{-1}}$ and $c_v \approx 1.864\left(\mathrm{J\,g^{-1}K^{-1}}\right)$ are the specific heats of liquid water and vapor; $\rho_l \approx 1.0\mathrm{g\,cm^{-3}}$ is density of liquid water. Thus, $c_l\rho_l q_l(T-T_0)$ and $L_0\rho_l q_v + c_v\rho_l q_v(T-T_0)$ represent the sensible heat fluxes carried by liquid water, and the latent and sensible heat fluxes carried by vapor, relative to the internal energy of liquid water at T_0. Following that, $q_h(h,T)$ becomes the net soil heat flux.

The Philip and de Vries (1957) model is widely used in CHWT simulations, and multiple improvements and validations of such a model have been reported. For example, Nassar and Horton (1989, 1997) included the osmotic potential and provided a coupled heat, water, and solute transfer model in wettable soils. Heitman et al. (2007, 2008) used the Philip and de Vries (1957) model to investigate thermally driven soil water redistribution. Zeng et al. (2011b) included dry air flow and illustrated the impact of gas flow on heat and water exchanges between the atmosphere and shallow soil profiles. The derivations of the Philip and de Vries (1957) model can be found in Heitman et al. (2008) and Wang et al. (2017b), and detailed discussion on some soil hydraulic or thermal properties, e.g., λ and d_{tl}, can be found in Lu et al. (2014), Groenevelt and Kay (1974), Milly (1982) and Wang et al. (2022a). Two constitutive relations are implicitly assumed in Eq. (1). One is the soil water characteristic curve, representing the relationship between h and θ, and the other one represents how $k(h,T)$ varies with respect to h and T, with the given saturated hydraulic conductivity $k_{sat}\left(\mathrm{cm\,s^{-1}}\right)$.

In this study, spatial heterogeneities are assumed for both k_{sat} and λ. From the experimental perspective, such spatial heterogeneities can be obtained by geospatial investigations. For numerical modeling, 2D random fields with pre-specified marginal distributions and spatial covariances are used to represent the spatial variabilities (Simunek et al., 1992). Hereafter, we use upper-case letters to represent coefficients with spatial randomness, and lower-case letters to represent deterministic coefficients. Therefore, replacing $k(h,T)$, k_{sat}, $d_{tl}(h,T)$ [$d_{tl}(h,T)$ is related to $k(h,T)$, see the appendix in Wang et al. (2022a)] and λ in Eq. (1) by $K(h,T)$, K_{sat}, $D_{tl}(h,T)$ and Λ gives the following governing equations.

$$\begin{cases} \textit{Water equation}: c_{\theta\theta}\dfrac{\partial h}{\partial t} + c_{\theta T}\dfrac{\partial T}{\partial t} = \nabla\cdot[(K(h,T) + d_{mv}(h,T))\nabla h + (d_{tv}(h,T) + D_{tl}(h,T))\nabla T] & (2a) \\ \textit{Heat equation}: c_{T\theta}\dfrac{\partial h}{\partial t} + c_{TT}\dfrac{\partial T}{\partial t} = -\nabla\cdot[-\Lambda\nabla T + c_l\rho_l q_l(T-T_0) + [L_0\rho_l q_v + c_v\rho_l q_v(T-T_0)]] & (2b) \end{cases}$$

2.2. Formulations of the spatial variability of K_{sat} and Λ

For K_{sat} and Λ, suppose that the random portions and the deterministic portions can be separated, i.e.,

$$K_{sat}(\vec{x}) = C_{K_{sat}}(\vec{x})k_{sat}, \Lambda(\vec{x}) = C_{\Lambda}(\vec{x})\lambda \quad (3)$$

where $\vec{x} \in \Omega$ indicates the spatial position in a given soil sample. Then, constructing 2D random fields of K_{sat} and Λ can be reduced to creating the two random fields for the coefficients, $C_{**}(\vec{x})$ s on Ω, where $** = K_{sat}, \Lambda$.

If $C_{**}(\vec{x}) \sim N(\mu_{**} = 0, \sigma^2_{**})$, with a pre-defined spatial covariance, the Karhunen-Loeve (KL) expansion can be employed. The intuition of the KL expansion is to separate the randomness and the spatial locations. Suppose $C_{**}(\vec{x})$ are wide-sense stationary, such that the spatial covariance can be expressed with a kernel that only takes the distance between two positions $\vec{x_1}, \vec{x_2} \in \Omega$ [i.e., $\mathrm{dist}(\vec{x_1}, \vec{x_2})$] and a correlation length (η, cm) as inputs,

$$\mathbb{E}[C_{**}(\vec{x_1})C_{**}(\vec{x_2})] = \sigma^2_{**}exp\left(-\frac{dist(\vec{x_1},\vec{x_2})}{\eta_{**}}\right), where ** = K_{sat}, \Lambda \quad (4)$$

Then, $C_{**}(\vec{x})$ can be expanded by a group of (uncorrelated) random variables $\{\xi_n\}_{n\in\mathbb{N}}$ and a group of spatial deterministic functions $f_n(\vec{x})$,

$$C_{**}(\vec{x}) = \sum_{n\in\mathbb{N}}\sqrt{\varpi_n}\xi_n f_n(\vec{x}), \text{ where } ** = K_{sat}, \Lambda \quad (5)$$

$\{\varpi_n, f_n(\vec{x})\}_{n\in\mathbb{N}}$ are the eigenvalues and the (orthonormal) eigenfunctions of the covariance kernel in Eq. (4). $\{\varpi_n, f_n(\vec{x})\}_{n\in\mathbb{N}}$ can be determined via a characteristic equation shown in Eq. (6), which is also known as the homogeneous Fredholm integral equation of the second kind.

$$\{\varpi_n, f_n(\vec{x})\}_{n\in\mathbb{N}} : \underbrace{\int_\Omega \sigma^2_{**}\exp\left(-\frac{\mathrm{dist}(\vec{x_1},\vec{x_2})}{\eta_{**}}\right)f_n(\vec{x_1})d\vec{x_1} = \varpi_n f_n(\vec{x_2})}_{\text{characteristic equation}} \quad \text{and} \int_\Omega f_i(\vec{x})f_j(\vec{x})d\vec{x} = \delta_{ij}$$
$$\{\xi_n\}_{n\in\mathbb{N}} : \xi_n \sim \mathcal{N}(\mu = 0, \sigma^2 = 1) \quad \text{and } \mathbb{E}[\xi_m\xi_n] = 0, \quad \forall m \neq n \quad (6)$$

where δ_{ij} is the Kronecker symbol. Solving Eq. (6) is the critical step in implementing the KL expansion, and we provide two illustrative examples.

Example 2.1. ***(Manhattan distance)***.

Let $\Omega = [0,L]\times[0,L]$, $\vec{x_1} = (x_1,y_1)$, $\vec{x_2} = (x_2,y_2) \in \Omega$, and define the Manhattan distance as $\mathrm{dist}(\vec{x_1},\vec{x_2}) \underset{\text{def}}{=} |x_1-x_2| + |y_1-y_2|$. The covariance kernel becomes $\sigma^2\exp[-(|x_1-x_2|+|y_1-y_2|)/\eta]$, and the eigenvalues and eigenfunctions can be solved analytically.

Starting with $\exp(-|x_1-x_2|/\eta)$, assume $f(x) = \eta w\cos wx + \sin wx$, and we can obtain $\int_0^L \exp\left(-\frac{|x_1-x_2|}{\eta}\right)f(x_1)dx_1 = \frac{2\eta f(x_2)}{1+\eta^2w^2} + \frac{\eta}{1+\eta^2w^2}\exp\left(-\frac{L-x_2}{\eta}\right)\left[\left(\eta^2w^2-1\right)\sin wL - 2\eta w\cos wL\right]$. Compared this integral with the characteristic equation in Eq. (6), the eigenvalues and eigenfunctions of $\exp(-|x_1-x_2|/\eta)$, i.e., $\left\{\widetilde{\varpi_n}, \widetilde{f_n(x)}\right\}_{n\in\mathbb{N}}$, can be observed as,

$$\widetilde{\varpi_n} = \frac{2\eta}{1+\eta^2 w_n^2}, \widetilde{f_n(x)} = \frac{1}{A_n}[\eta w_n \cos w_n x + \sin w_n x]$$

where $\{w_n\}_{n\in\mathbb{N}}$ satisfies $(\eta^2 w^2 - 1)\sin wL - 2\eta w \cos wL = 0$, and $A_n = \left[\int_0^L [\eta w_n \cos w_n x + \sin w_n x]^2 dx\right]^{1/2} = \left[(\eta^2 w_n^2 + 1)L/2 + \eta\right]^{1/2}$ are the normalizers for $\widetilde{f_n(x)}$.

Following the result above, for $\sigma^2 \exp(-\text{dist}(\overrightarrow{x_1}, \overrightarrow{x_2})/\eta) = \sigma^2 \exp[-(|x_1 - x_2| + |y_1 - y_2|)/\eta]$,

$$\begin{aligned}
&\iint_{\Omega=[0,L]^2} \sigma^2 \exp\left(-\frac{\text{dist}(\overrightarrow{x_1}, \overrightarrow{x_2})}{\eta}\right) \widetilde{f_m(x_1)} \widetilde{f_l(y_1)} dx_1 dy_1 \\
&= \sigma^2 \int_0^L \exp\left(-\frac{|x_1 - x_2|}{\eta}\right) \widetilde{f_m(x_1)} dx_1 \int_0^L \exp\left(-\frac{|y_1 - y_2|}{\eta}\right) \widetilde{f_l(y_1)} dy_1 \\
&= \sigma^2 \widetilde{\varpi_m} \widetilde{f_m(x_2)} \times \widetilde{\varpi_l} \widetilde{f_l(y_2)} = \underbrace{\widetilde{\varpi_m}\widetilde{\varpi_l}}_{\varpi_n} \sigma^2 \times \underbrace{\widetilde{f_m(x_2)} \widetilde{f_l(y_2)}}_{f_n(\overrightarrow{x})}
\end{aligned}$$

Thus, the eigenvalues and eigenfunctions of $\exp(-\text{dist}(\overrightarrow{x_1}, \overrightarrow{x_2})/\eta)$, i.e., $\{\varpi_n, f_n(\overrightarrow{x})\}_{n\in\mathbb{N}}$, becomes $\left\{\widetilde{\varpi_m}\widetilde{\varpi_l}\sigma^2, \widetilde{f_m(x)}\widetilde{f_l(y)}\right\}_{m,l\in\mathbb{N}}$, where $\left\{\widetilde{\varpi_m}, \widetilde{f_m(x)}\right\}_{m\in\mathbb{N}}$ and $\left\{\widetilde{\varpi_l}, \widetilde{f_l(y)}\right\}_{l\in\mathbb{N}}$ are the eigenvalues and eigenfunctions of $\exp(-|x_1 - x_2|/\eta)$ and $\exp(-|y_1 - y_2|/\eta)$, respectively.

△.

Example 2.2. ***(Euclidean distance)***.

Let $\Omega = [0, L] \times [0, L]$, $\overrightarrow{x_1} = (x_1, y_1)$, $\overrightarrow{x_2} = (x_2, y_2) \in \Omega$, and define the Euclidean distance as $\text{dist}(\overrightarrow{x_1}, \overrightarrow{x_2}) \overset{\text{def}}{=} \|\overrightarrow{x_1} - \overrightarrow{x_2}\| = \sqrt{(x_1 - x_2)^2 + (y_1 - y_2)^2}$. The covariance kernel becomes $\sigma^2 \exp(-\|\overrightarrow{x_1} - \overrightarrow{x_2}\|/\eta)$. Compared to the Manhattan distance, the Euclidean distance is more natural in physical applications. However, analytically solving the eigenvalues and eigenfunctions can be challenging. Hence, a semi-analytic method via 2D Fourier expansion was proposed in Li et al. (2006). Suppose the 2D Fourier expansion of the eigen function can be expressed as.

$$f_n(\overrightarrow{x}) \overset{\text{def}}{=} \sum_{i=0}^N c_i \varphi_i(x, y)$$

For simplicity, we use c_i and $\varphi_i(x, y)$ to represent the Fourier coefficients and the 2D trigonometric bases, where $\varphi_i(x, y) \neq 0$ are orthonormal with respect to i.

The characteristic equation implies.

$$\iint_\Omega \sigma^2 \exp\left(-\frac{\|\overrightarrow{x_1} - \overrightarrow{x_2}\|}{\eta}\right) \sum_{i=0}^N c_i \varphi_i(x_1, y_1) dx_1 dy_1 = \varpi_n \sum_{j=0}^N c_j \varphi_j(x_2, y_2)$$

Multiply both side by $\varphi_k(x_2, y_2), k = 1, 2, \cdots, N$ and integrate over Ω,

$$\sum_{i=0}^N c_i \underbrace{\left[\sigma^2 \iint_\Omega \varphi_k(x_2, y_2) \iint_\Omega \exp\left(-\frac{\overrightarrow{x_1} - \overrightarrow{x_2}}{\eta}\right) \varphi_i(x_1, y_1) dx_1 dy_1 dx_2 dy_2\right]}_{=\Phi_{k,i}} = \varpi_n c_k$$

Therefore, the characteristic equation can be reformulated into a linear system, $\Phi \widetilde{c} = \varpi \widetilde{c}$, where $\Phi = [\Phi_{k,i}] \in \mathbb{R}^{N\times N}$ and $\widetilde{c} = [c_k] \in \mathbb{R}^N$, and determining the eigenvalues and eigenfunctions can be transformed to computing the eigenvalues and eigenvectors of matrix Φ.

△.

In soil physics studies, K_{sat} and Λ, hence $C_{**}(\overrightarrow{x})$ s, are usually assumed to follow lognormal distributions. Therefore, the KL expansion should be modified as an iterative method (Phoon et al. 2002; Dai et al., 2019), such that the marginal distribution at each spatial position follows the desired lognormal distributions. The intuition of the iterative method is to use distribution transformations to approach the marginal distribution (i.e., the lognormal distribution in this study), and use Latin hypercube sampling (or similar methods) to un-correlate the random seeds $\{\xi_n\}_{n\in\mathbb{N}}$ in the KL expansion [see Eq. (5)]. The iterative method can be summarized as follows.

(a) Assume $C_{**}(\overrightarrow{x}) \sim \text{Lognormal}(\mu_{**} = 1, \sigma_{**}^2)$. Define a "shifted lognormal distribution" as $D_{**}(\overrightarrow{x}) = C_{**}(\overrightarrow{x}) - 1$, such that the expectation and variance of $D_{**}(\overrightarrow{x})$ are 0 and σ_{**}^2. Generate M realizations of random numbers, i.e., $\{\xi_n(m)\}_{n\in\mathbb{N}, m=1,2,\cdots,M}$, as the initial samples based on the distribution of $D_{**}(\overrightarrow{x})$.

(b) Compute the random fields $D_{**}^p(\overrightarrow{x}, m)$ with Eq. (7), where p represents the number of iterations.

$$D_{**}^p(\overrightarrow{x}, m) = \sum_{n\in\mathbb{N}} \sqrt{\varpi_n} \xi_n(m) f_n(\overrightarrow{x}), \text{ where } ** = K_{sat}, \Lambda, \ m = 1, 2, \cdots, M \quad (7)$$

(c) For a specific position $\overrightarrow{x}^\# \in \Omega$, assume the empirical cumulative distribution functions of the marginal distribution of $D_{**}^p(\overrightarrow{x}^\#, m)$ and the shifted log-normal distribution are $F_{D_{**}^p}^\#$ and $F_{\text{Log}\mathcal{N}}$, respectively. The random vector $\{D_{**}^p(\overrightarrow{x}^\#, m)\}_{m=1,2,\cdots,M}$ can be

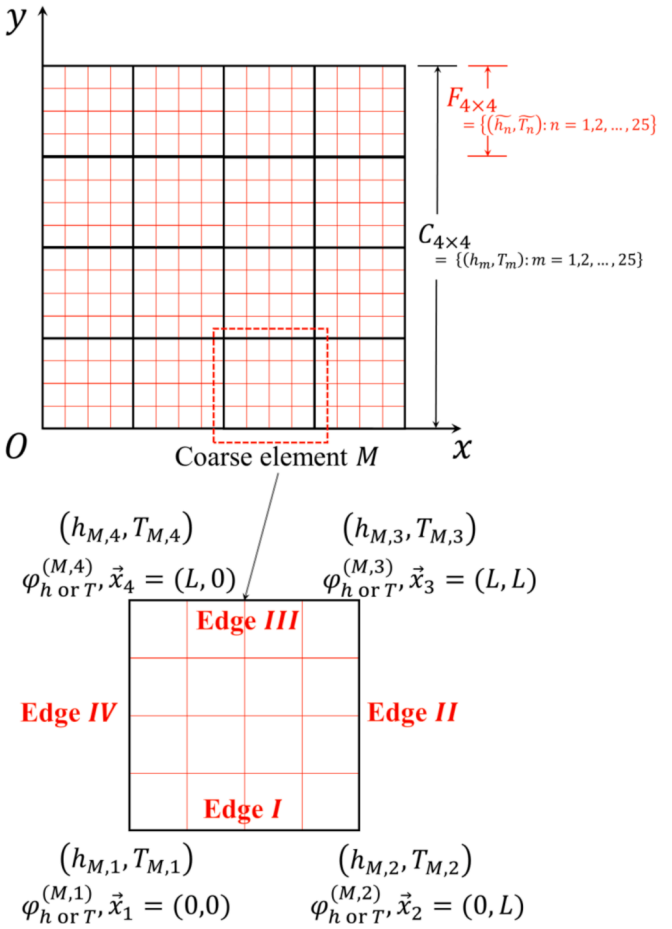

Fig. 1. An example spatial discretization used to develop the MsFEM scheme. In the upper figure, the black lines demarcate a 4×4 coarse grid, where each black box presents a coarse element. A coarse element is further divided into a 4×4 fine grid. Hereafter, we use $C_{m\times m}F_{n\times n}$ to define the MsFEM spatial grid, and $m = n = 4$ in the upper figure. In the lower figure, we emphasize one coarse element $\vec{x}_1\vec{x}_2\vec{x}_3\vec{x}_4$, where $\varphi_{h\text{ or }T}^{(M,i)}$, $i = 1, 2, 3, 4$ are MsFEM basis functions for soil water potential (h) or soil temperature (T) at the four coarse nodes, and the four edges (Edges I, II, III, and IV), which will be used to embed boundary conditions for $\varphi_{h\text{ or }T}^{(M,i)}$, are labeled in a counterclockwise direction.

transformed from its empirical distribution to the shifted log-normal marginal distribution using Eq. (8).

$$\widetilde{D^p_{**}}(\vec{x}^{\#},\, m) = F^{-1}_{\mathrm{Log}\mathscr{N}}\left[F^{\#}_{D^p_{**}}\left[D^p_{**}(\vec{x}^{\#},\, m)\right]\right], \text{where } ** = K_s, \Lambda; m = 1, 2, \cdots, M; \vec{x}^{\#} \in \Omega \tag{8}$$

Then, $\xi_n(m)$ can be updated using Eq. (9), where $\mathbb{E}_M$ indicates the expectation is taken with respect to the number of realizations (M).

$$\xi_n(m) \leftarrow \frac{1}{\sqrt{\varpi_n}}\int_{\Omega}\left[\widetilde{D^p_{**}}(\vec{x},\, m) - \mathbb{E}_M\left[\widetilde{D^p_{**}}(\vec{x},\, m)\right]\right] f_n(\vec{x})\, d\vec{x}, \text{where } m = 1, 2, \cdots, M \tag{9}$$

Without loss of generality, $\{\xi_n(m)\}_{n\in\mathbb{N}, m=1,2,\cdots,M}$ has zero mean and unit variance. Otherwise, $\{\xi_n(m)\}_{n\in\mathbb{N}, m=1,2,\cdots,M}$ can be simply standardized with respect to m. Possible correlations of $\{\xi_n(m)\}_{n\in\mathbb{N}, m=1,2,\cdots,M}$ with respect to n can be reduced following the method similar to Latin hypercube sampling, proposed in Phoon et al. (2005), where the correlations are measured with Pearson product-moment rather than Spearman rank method.

(d) Redo the computation of Eq. (7) using the updated $\{\xi_n(m)\}_{n\in\mathbb{N}, m=1,2,\cdots,M}$, and repeat Eqs. (7)-(9) for p iterations, until the marginal distribution of $D^p_{**}(\vec{x}, m)$ at $\forall\vec{x} \in \Omega$ approximates the target, shifted log-normal distribution. Then, $C_{**}(\vec{x}) = D^p_{**}(\vec{x}, m) + 1$ is the desired random field. Although Phoon et al. (2005) strove to suppress the undesired heavy tails in the simulated marginal distributions, in practice, they may not be totally removed and need to be truncated at the end of the construction.

2.3. Construction of the MsFEM scheme

Recall the two ingredients of MsFEM are the basis functions and the global formulations. The basis functions are determined in a fine grid to capture the small-scale soil properties, while the global formulations are established in a coarse grid to solve the governing equations [Eq. (2)]. To clarify this exposition, we first present a discretization of the spatial domain that includes a coarse grid and a fine grid. In Fig. 1, the spatial domain is first discretized into a 4×4 coarse grid ($C_{4\times4}$) and each coarse element is further discretized into a 4×4 fine grid ($F_{4\times4}$). Hereafter, we use the format "$C_{m\times m}F_{n\times n}$" to describe the MsFEM grids. In the MsFEM grids, $(h_{M,i}, T_{M,i})$ is used to denote the nodal values of the soil water potential and soil temperature for a coarse element $M \in C_{m\times m}$ and coarse node $i, i = 1, 2, 3, 4$, see the lower diagram in Fig. 1. $(\widetilde{h}, \widetilde{T})$ is used to represent the nodal soil water potential and soil temperature in the fine grid. For standard FEM, only one scale is considered, and the grid can be presented as "$C_{m\times m}$". In this study, when a grid is expressed in the format "$C_{m\times m}F_{n\times n}$", MsFEM will be used as the numerical solver; when a grid is expressed in the format "$C_{m\times m}$", the associated numerical method will be the standard FEM.

For a given coarse element M (Fig. 1), the basis functions, namely $\varphi^{(M,i)}, i = 1,2,3,4$, can be solved based on the fine grid within the given coarse element. In standard FEM, bilinear functions are usually adopted as the basis functions, and we include them into a functional space $\mathscr{V}^0 = \left\{\varphi_0^{(M,i)}\right\}_{M\in C_{m\times m}, i=1,2,3,4}$. In order to represent the spatial variabilities of K_{sat} and Λ, two groups of MsFEM basis functions must be obtained by solving the following homogeneous equations.

$$\begin{cases} \nabla\bullet\left[K_{sat}\nabla\varphi_h^{(M,i)}\right] + \zeta\nabla\bullet\left[D_{tl,sat}\nabla\varphi_T^{(M,i)}\right] = 0 & (10a) \\ \nabla\bullet\left[\Lambda\nabla\varphi_T^{(M,i)}\right] = 0 & (10b) \end{cases}$$

$\varphi_h^{(M,i)}$ represents the MsFEM basis functions for soil water potential and $\varphi_T^{(M,i)}$ represents the MsFEM basis functions for soil temperature, which satisfy $\varphi_h^{(M,i)}\left(\vec{x}_j\right) = \varphi_T^{(M,i)}\left(\vec{x}_j\right) = \delta_{ij}, i, j = 1, 2, 3, 4$ (see Fig. 1, lower diagram). $D_{tl,sat}$ is the saturated value of $D_{tl}(h, T)$ with the initial soil temperature. Equation (10a) indicates that $\varphi_h^{(M,i)}$ and $\varphi_T^{(M,i)}$ are correlated, and the effects of spatial variations in K_{sat} and Λ on the CHWT model are not independent. We denote two functional spaces for the MsFEM basis functions as $\mathscr{V}^h = \left\{\varphi_h^{(M,i)}\right\}_{M\in C_{m\times m}, i=1,2,3,4}$ and $\mathscr{V}^T = \left\{\varphi_T^{(M,i)}\right\}_{M\in C_{m\times m}, i=1,2,3,4}$. $\zeta \approx 0.01$ is an empirical scaling factor. From a mathematical perspective, ζ is used to ensure that $\varphi_h^{(M,i)} \geq 0$ and $\varphi_T^{(M,i)} \geq 0$. From a physical perspective, ζ exists because (a) the soil water potential has a scale of $10^3 - 10^4$cm and changes nonlinearly with respect to soil water content, while the soil temperature has a scale of 10^1°C; (b) based on measurements, the liquid water flow under temperature gradient is typically < 5% of the liquid water flow under water potential gradient (Prunty, 2009).

The values of the MsFEM basis functions along the boundaries of the coarse element M, namely Edges I, II, III, and IV, can reflect the goodness of the basis functions in representing the small-scale soil properties, and significantly affect the accuracy of the global MsFEM scheme. Failing to correctly define the boundary conditions may cause interactions between the soil heterogeneities and the coarse grid size, and lead to errors known as "scale resonance" (Hou and Wu, 1997). Applying the oscillatory boundary conditions, i.e., a 1D form of Eq. (10) along the four edges, or an oversampling technique can ameliorate the behaviors of the MsFEM basis functions, and He and Ren (2006) showed that both methods produce similar improvements in soil water transfer modeling. In this study, we focus on the oscillatory boundary conditions because they can be easily expressed with analytical solutions and lead to a

Table 1
Soil Physical Properties for Examples 2.3 and 2.4.

Ida (fine-silty, mixed, superactive, calcareous, mesic Typic Udorthents)	
Soil Textural Properties	
Sand (f_{sand}, g g^{-1})	0.022
Silt (f_{silt}, g g^{-1})	0.729
Clay (f_{clay}, g g^{-1})	0.249
Organic matter (g g^{-1})	0.044
Specific surface area (S_a, cm^2 cm^{-3})†	2.44 × 10^6
Bulk density (ρ_b, g cm^{-3})	1.20
Hydraulic Properties	
Saturated water content (θ_{sat}, cm^3 cm^{-3})	0.547
Saturated hydraulic conductivity at T_0 (k_{sat}, cm s^{-1})	3.80 × 10^{-5}
Water characteristic function	$h = -13.0 \times (\theta/\theta_s)^{-6.53}$
Hydraulic conductivity (k, cm s^{-1})	$k = [\mu(T_0)/\mu(T)] \times (\theta/\theta_s)^{16.06} k_{sat}$‡
Thermal Properties	
Thermal conductivity (λ, W cm^{-1} K^{-1}) (Lu et al., 2014)	$\lambda = 0.01(\lambda_{dry} + \exp(\beta - \theta^{-\alpha}))$ $\lambda_{dry} = -0.56\theta_s + 0.51$ $\alpha = 0.67 f_{clay} + 0.24$ $\beta = 1.97 f_{sand} + 1.87\rho_b - 1.36 f_{sand}\rho_b - 0.95$

† The specific surface area is defined for a unit soil volume, i.e., 1 cm^3.
‡ $\mu(T)$ represents the dynamic viscosity of water, as a function of soil temperature.

conforming FEM scheme in the global formulation.

For instance, along Edge I in coarse element M, where $\vec{x} = (x, 0)$, $x \in [0, L]$, the boundary values of $\varphi_h^{(M,1)}(\vec{x})$ and $\varphi_T^{(M,1)}(\vec{x})$ satisfy a 1D elliptic equation system degraded from Eq. (10), i.e.,

$$\begin{cases} \dfrac{\partial}{\partial x} K_{sat} \dfrac{\partial}{\partial x} \varphi_h^{(M,1)} + \zeta \dfrac{\partial}{\partial x} D_{tl,sat} \dfrac{\partial}{\partial x} \varphi_T^{(M,1)} = 0 \\ \dfrac{\partial}{\partial x} \Lambda \dfrac{\partial}{\partial x} \varphi_T^{(M,1)} = 0 \end{cases} \tag{11}$$

At the two ending points of Edge I, $\vec{x}_1 = (0, 0)$ and $\vec{x}_2 = (0, L)$ (see Fig. 1, lower diagram), $\varphi_h^{(M,1)}(\vec{x}_1) = \varphi_T^{(M,1)}(\vec{x}_1) = 1$ and $\varphi_h^{(M,1)}(\vec{x}_2) = \varphi_T^{(M,1)}(\vec{x}_2) = 0$. Then, the solution to Eq. (11) can be calculated analytically.

$$\begin{cases} \varphi_h^{(M,1)}(x,0) = 1 + \dfrac{\zeta}{\int_0^L \frac{1}{\Lambda} ds} \int_0^x \dfrac{D_{tl}(h,T)}{K(h,T)\Lambda} ds - \left[\dfrac{1}{\int_0^L \frac{1}{K(h,T)} ds} + \dfrac{\zeta}{\int_0^L \frac{1}{K(h,T)} ds \int_0^L \frac{1}{\Lambda} ds} \int_0^L \dfrac{D_{tl}(h,T)}{K(h,T)\Lambda} ds \right] \int_0^x \dfrac{1}{K(h,T)} ds \\ \varphi_T^{(M,1)}(x,0) = 1 - \dfrac{1}{\int_0^L \frac{1}{\Lambda} ds} \int_0^x \dfrac{1}{\Lambda} ds \end{cases} \tag{12}$$

$$\begin{cases} \sum_{m \in C_{m\times m}} \sum_{i=1,2,3,4} \left[c_{\theta\theta} \dfrac{\partial h_{M,i}}{\partial t} \iint_\Omega \varphi_h^{(M,i)} \psi d\omega + c_{\theta\theta} \dfrac{\partial T_{M,i}}{\partial t} \iint_\Omega \varphi_T^{(M,i)} \psi d\omega \right] \\ = - \sum_{m \in C_{m\times m}} \sum_{i=1,2,3,4} \left[(K + d_{mv}) h_{M,i} \iint_\Omega \nabla \varphi_h^{(M,i)} \cdot \nabla \psi d\omega + (d_{tv} + D_{tl}) T_{M,i} \iint_\Omega \nabla \varphi_T^{(M,i)} \cdot \nabla \psi d\omega \right] \\ - \underbrace{\int_{\partial\Omega} (q_k^{\mathrm{Ext}} + q_k^{\mathrm{Ext}}) \psi dl}_{\text{external water or vapor fluxes as boundary conditions}} \qquad \forall \psi \in v^0 \end{cases} \tag{13a}$$

$$\begin{cases} \sum_{m \in C_{m\times m}} \sum_{i=1,2,3,4} \left[c_{T\theta} \dfrac{\partial h_{M,i}}{\partial t} \iint_\Omega \varphi_h^{(m,i)} \psi d\omega + c_{TT} \dfrac{\partial T_{M,i}}{\partial t} \iint_\Omega \varphi_T^{(M,i)} \psi d\omega \right] \\ = - \sum_{m \in C_{m\times m}} \sum_{i=1,2,3,4} \left[\Lambda h_{M,i} \iint_\Omega \nabla \varphi_T^{(M,i)} \cdot \nabla \psi d\omega \right] + \iint_\Omega \left[c_l p_l q_l (T_{up} - T_0) + \left[L_0 p_l q_v + c_v p_l q_v (T_{up} - T_0) \right] \right] \cdot \nabla \psi d\omega \\ - \underbrace{\int_{\partial\Omega} q_h^{\mathrm{Ext}} \psi dl}_{\text{external conductive heat fluxes as boundary conditions}} \underbrace{- \int_{\partial\Omega} \left[c_l p_l q_l (T_{up} - T_0) + \left[L_0 p_l q_v + c_v p_l q_v (T_{up} - T_0) \right] \right] \psi dl}_{\text{exernal sensible and latent heat fluxes as boundary conditions}} \quad \forall \psi \in v^0 \end{cases} \tag{13b}$$

After solving $\varphi_h^{(M,1)}(\vec{x})$ and $\varphi_T^{(M,1)}(\vec{x})$ along Edge I, the values of $\varphi_h^{(M,2)}(\vec{x})$ and $\varphi_T^{(M,2)}(\vec{x})$ along Edge I can be obtained via $\varphi_h^{(M,2)}(\vec{x}) = 1 - \varphi_h^{(M,1)}(\vec{x})$ and $\varphi_T^{(M,2)}(\vec{x}) = 1 - \varphi_T^{(M,1)}(\vec{x})$, respectively. In addition, $\varphi_h^{(M,3)}(\vec{x}) = \varphi_T^{(M,3)}(\vec{x}) = \varphi_h^{(M,4)}(\vec{x}) = \varphi_T^{(M,4)}(\vec{x}) = 0$ along Edge I, similar to the requirements in standard FEM.

The procedures can be repeated for Edges II, III, and IV. In practice, since h and T (hence K_{sat}, $D_{tl,sat}$ and Λ) are discretized in the spatial domain Ω, the boundary values of the basis function can also be solved numerically. Based on the choice of the boundary conditions, it is easy to show that $\sum_{i=1,2,3,4} \varphi_h^{(M,i)}(\vec{x}) \equiv \sum_{i=1,2,3,4} \varphi_T^{(M,i)}(\vec{x}) \equiv 1$, $\forall \vec{x}$ in the coarse element (M).

The target of the global formulation is to transform the governing equations [Eq. (2)] into a discretized scheme and solve the nodal soil water potential and temperature (h_m, T_m) [or equivalently, soil water content and temperature (θ_m, T_m)] on the coarse grid $C_{m\times m}$ (see Fig. 1, upper diagram), where the small-scale variabilities of soil properties are accounted for by the MsFEM basis functions. Since we have two groups of MsFEM basis functions $\mathscr{V}^h$ and $\mathscr{V}^T$, Petrov-Galerkin FEM can be used as the global formulation (Hou et al., 2004; Reddy, 2006). Let $\sum_{M \in C_{m\times m}} \left[\sum_{i=1,2,3,4} h_{M,i} \varphi_h^{(M,i)} \right]$ and $\sum_{M \in C_{m\times m}} \left[\sum_{i=1,2,3,4} T_{M,i} \varphi_T^{(M,i)} \right]$ be the MsFEM trial solutions for the soil water potential and the soil temperature, where $h_{M,i}$ and $T_{M,i}$ are the nodal values. The global formulation derived from Eq. (2) are shown as follows.

On the right-hand side of Eq. (13b), T is replaced by the temperature from the upwind direction, i.e., T_{up}, for the advective heat fluxes. The time domain differentiation can be discretized using an explicit or an implicit Euler scheme. Because the MsFEM basis functions $\varphi_h^{(M,i)}$ and $\varphi_T^{(M,i)}$ can be pre-determined for each coarse element using Eqs. (10)-(12), all of the integrals shown in Eq. (13) can be pre-calculated. Therefore, compared to the standard FEM, the MsFEM scheme proposed in this study does not requires additional computing loads, except for the time spent in initializing the MsFEM basis functions at the beginning of the simulation.

After obtaining the solutions on the coarse grid, the MsFEM basis functions can be used to reconstruct the fine grid soil water potential and temperature, where the $\vec{x}$ can take the positions of fine grid nodes.

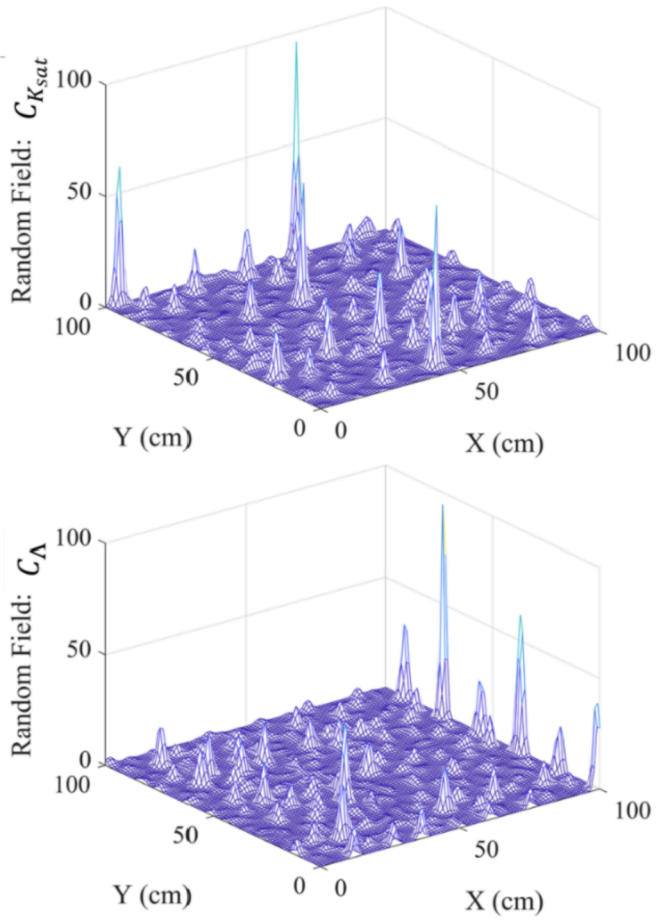

Fig. 2. The two 2D random fields $C_{K_{sat}}$ and C_Λ in Example 2.3.

$$\widetilde{h} = \sum_{M\in C_{m\times m}} \left[\sum_{i=1,2,3,4} h_{M,i}\varphi_h^{(M,i)}(\vec{x}) \right], \widetilde{T} = \sum_{M\in C_{m\times m}} \left[\sum_{i=1,2,3,4} T_{M,i}\varphi_T^{(M,i)}(\vec{x}) \right] \quad (14)$$

However, the motivation of the MsFEM scheme is to use basis functions to absorb the small-scale soil variabilities, such that soil water potential and temperature can be solved for large-scale applications without resolving small-scale features. Hence, reconstruction of the fine grid values is not the priority of the MsFEM scheme in this study.

2.4. Illustrative Example

In this section, we provide examples to demonstrate the efficacy of the model presented in Sections 2.1 to 2.3. Applications of MsFEM on soil liquid water transfer have been reported in multiple studies [e.g., He and Ren (2005; 2006)]. Therefore, in the following examples, we focus on applications of the MsFEM scheme on CHWT problems, emphasizing on the thermally driven water flux.

Example 2.3. (*Soil water redistribution under temperature gradients*).

Consider a $\Omega = [0,\ 100\,\text{cm}] \times [0, 100\,\text{cm}]$ horizontally placed soil sample, and the soil physical properties are listed in Table 1. The 2D random fields that simulate the spatial variabilities of K_{sat} and Λ are lognormally distributed, and a covariance kernel based on the Manhattan distance (see Example 2.1) is used with the random variables $\xi \sim \text{Lognormal}(\mu = 1, \sigma^2 = 10^4)$ and $\eta = 5\,\text{cm}$. The lognormal distribution is truncated below the 0.01 fractile and above the 0.99 fractile to prevent extreme values in the random fields (i.e., the tail distributions). Fig. 2 presents the two 2D random fields used in this example, namely $C_{K_{sat}}$ and C_Λ. The 2D random fields are positive and relatively uniform, with only a few spikes reaching values near 100.

The soil sample has an initial water content of $0.2\,\text{cm}^3\,\text{cm}^{-3}$ and an initial temperature of 25°C. The boundary of the soil sample is assumed to be impermeable for liquid water and vapor transfer, and two steady boundary temperatures, 20°C and 30°C, are imposed on the two opposite edges of the soil sample. The MsFEM grid used for this simulation is $C_{20\times20}F_{5\times5}$, and a 10-day simulation of soil water and temperature redistribution is performed.

The soil water content and temperature on both coarse and fine grids at the 10th day in the simulation are presented in Fig. 3. The soil water content near the low temperature edge ($y = 0\text{cm}$) reaches the highest

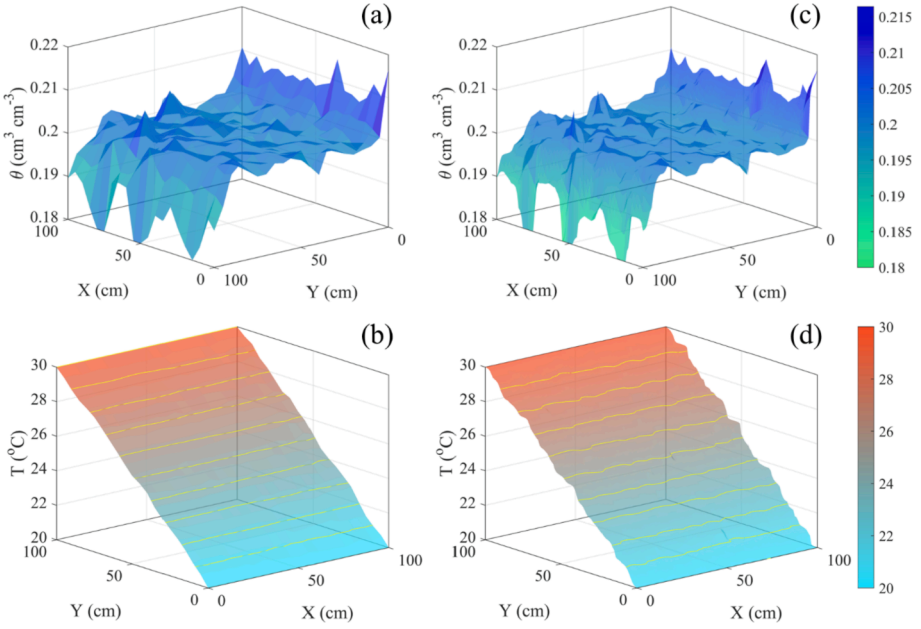

Fig. 3. The simulation results of soil water content and temperature using the MsFEM scheme and the $C_{20\times20}F_{5\times5}$ grid. The soil water content and temperature on the coarse grid are shown in (a) and (b); while the reconstructed soil water content and temperature on the fine grid are shown in (c) and (d). For presentation, the coordinate systems in (a, c) and the coordinate systems in (b, d) are not placed in the same direction. To emphasize the details in the soil temperature variations, contour plots are provided in (b, d).

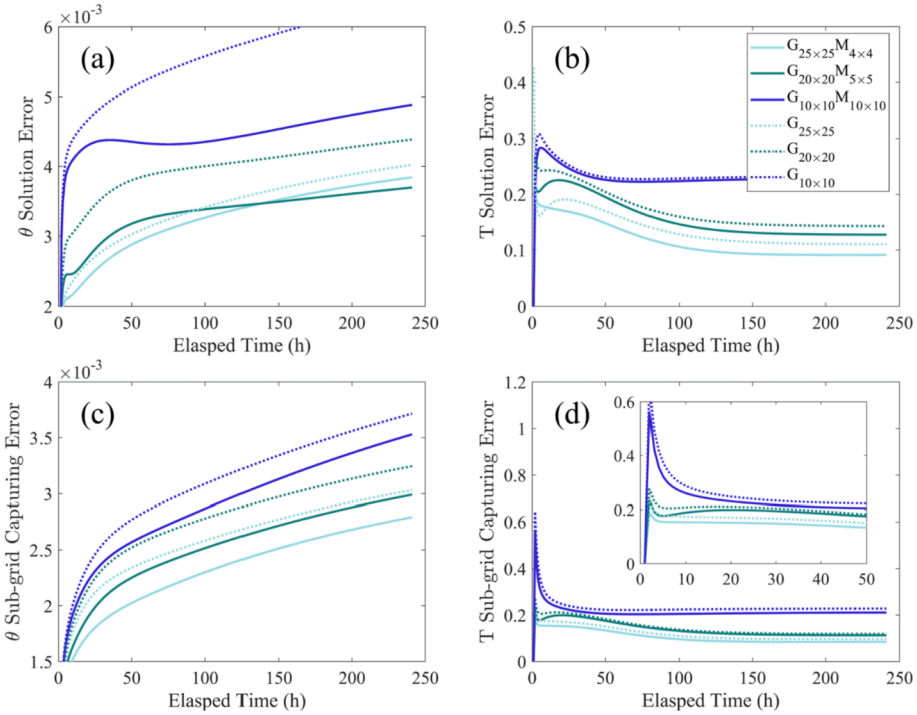

Fig. 4. The evolution of RMSE with respect to time, including (a) the solution error in soil water content, (b) the solution error in soil temperature, (c) the "sub-grid capturing error" in soil water content, and (d) the "sub-grid capturing error" in soil temperature. The MsFEM results are presented by solid lines with grids $C_{25\times25}F_{4\times4}$, $C_{20\times20}F_{5\times5}$ and $C_{10\times10}F_{10\times10}$. The standard FEM results are plotted by dashed lines with grids $C_{25\times25}$, $C_{20\times20}$ and $C_{10\times10}$. A small figure in (d) presents that for soil temperature, although the advantages of the MsFEM scheme in reducing the errors are limited, the "sub-grid capturing error" decreases faster compared to the standard FEM at the early stage of the simulation.

value; while near the high temperature edge ($y = 100$cm), the soil water content is relatively low. That is because water near the high temperature edge tends to vaporize, transfer under the temperature gradient, and condense near the low temperature edge, which is known as "thermally driven soil water flux". However, due to the heterogeneities in soil hydraulic conductivity, local fluctuations occur in the soil water content distribution. For Fig. 3a and c, the reconstructed soil water content in the fine grid is smoother than the soil water content distribution in the coarse grid. Some local maxima values in Fig. 3c are presented as "spikes" with relatively narrow spatial expansions. That is reasonable since the local maxima in K_{sat} and Λ are also "spikes" shown in Fig. 2. For Fig. 3b and d, the soil temperature distribution in the coarse grid changes almost linearly from the high temperature edge to the low temperature edge, and some small variations, presented by the

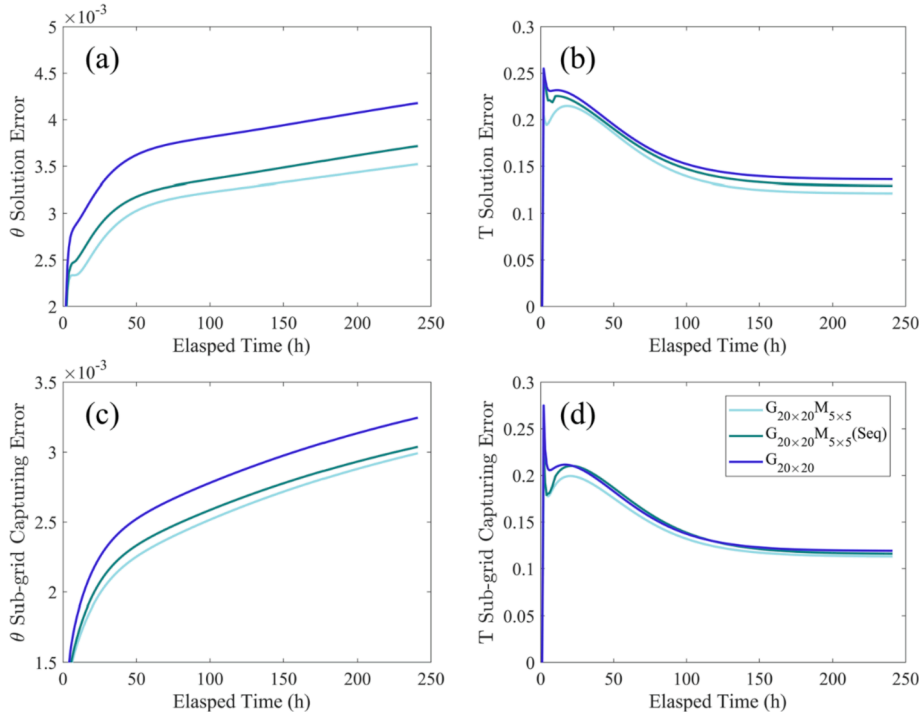

Fig. 5. The evolution of RMSE with respect to time for the three methods: the MsFEM scheme with $C_{20\times20}F_{5\times5}$ grid, the MsFEM sequential solver (Seq) with $C_{20\times20}F_{5\times5}$ grid, and the standard FEM with $C_{20\times20}$ grid, including (a) the solution error in soil water content, (b) the solution error in soil temperature, (c) the "sub-grid capturing error" in soil water content, and (d) the "sub-grid capturing error" in soil temperature.

contours, can only be observed when the fine grid temperature solution is reconstructed in Fig. 3d.

△.

Example 2.4. **(*Scale selection and error analyses*).**

For a given soil sample, if self-similarity is assumed or soil properties are represented with fractal methods (e.g., Shen et al., 2019; Jin et al., 2017), the characteristic scales of soil hydraulic conductivity and thermal conductivity may disappear. Therefore, in soil modeling, the choice of the coarse grid and the fine grid can be arbitrary, and may even depend on the scales where measurements are performed rather than the characteristic scales of the soil properties. Moreover, the small-scale features in K_{sat} and Λ only contain their local information, and intermediate structures, such as pore connectivity and tortuosity, may not be fully reflected based on the local variabilities of K_{sat} and Λ. Therefore, with the selected coarse and fine scales, some characteristics belonging to the intermediate scale can be missed. Thus, rather than saying the usage of the MsFEM basis functions is to capture the small-scale soil variabilities, it is more appropriate to claim the MsFEM basis functions are for computing the effective soil hydraulic and thermal properties.

Choosing a different spatial grid may exert effects on the CHWT simulation results. Therefore, in this example, we redo the simulation in Example 2.3 using MsFEM with three grids, $C_{25\times25}F_{4\times4}$, $C_{20\times20}F_{5\times5}$, $C_{10\times10}F_{10\times10}$, as well as using the standard FEM with grids $C_{25\times25}$, $C_{20\times20}$ and $C_{10\times10}$. To demonstrate the efficacy of the MsFEM scheme in "upscaling" the small-scale features, simulation results from the MsFEM scheme and the standard FEM scheme are compared. For reference, the soil water content and temperature on the underlying grid, $C_{100\times100}$, are simulated with the standard FEM scheme. The differences are expressed in two ways: (a) the root mean squared error (RMSE) of simulation results is calculated with the nodal values on the coarse grid, and (b) the RMSE of "sub-grid capturing (Efendiev and Hou, 2009)" is calculated on the underlying fine grid, related to the reference soil water content and temperature values solved on $C_{100\times100}$. Errors exist because we apply a discretized scheme to approximate the continuous governing equations. For the numerical scheme design, demarcating the error magnitudes, and studying how the errors change with respect to time are the critical issues. A desirable numerical scheme should have a relatively small error and a relatively small error growth rate with respect to time.

The evolution of errors with respect to time is presented in Fig. 4. Based on the MsFEM results, the simulation errors and the "sub-grid capturing errors" for soil water content are of the order 10^{-3}, and the errors for soil temperature are of the order 10^{-1}. Considering the initial water content $(0.2\,\mathrm{cm^3\,cm^{-3}})$ and the initial temperature of $(25^{\circ}\mathrm{C})$, the levels of relative errors of soil water content and soil temperature fall into the range of $10^{-3}-10^{-2}$, which are similar to the literature results (e.g., He and Ren, 2006).

For soil water content, the MsFEM scheme can increase the accuracy by as much as 30% compared to the standard FEM scheme, and the largest improvement of accuracy occurs on the $C_{10\times10}$ coarse grid (see Fig. 4a). That indicates the MsFEM basis functions can provide better representations of the effective soil hydraulic and thermal properties than the bilinear basis functions used in the standard FEM, when the mesh size of the coarse grid is relatively big.

For soil temperature, the advantage of using the MsFEM scheme is not profound. Two possible reasons are (a) the boundary conditions enforce a strong trend of soil temperature distribution; (b) more importantly, the magnitude of variations in Λ, with respect to soil water content and temperature, is smaller than that for K (i.e., K is more sensitive to the changes in soil water potential and temperature than Λ). Therefore, both the MsFEM and the standard FEM simulated temperature stably approach the steady state values at the end of the simulation, and the error values become constant with respect to time. However, we can still observe some benefits of MsFEM at the early stage of the simulation, where the errors in the MsFEM results decrease faster than the errors produced by the standard FEM scheme (see Fig. 4b, d and the small figure in Fig. 4d). Recall that in this study, the MsFEM basis functions are pre-calculated, so there is only a limited (or negligible) increase in the computing load to achieve the accuracy promotion via the MsFEM scheme.

△.

3. Partially coupled heat and water transfer and the MsFEM sequential solver

Implementation of MsFEM for CHWT simulations has been described in Section 2. However, for numerical applications, the heat and water transfer in soil is not always expressed as a fully coupled version, but rather as a partially coupled version. For example, in Hydrus, the two equations in Eq. (1) [or equivalently, in Eq. (2)] are solved one-by-one within a given time step (Saito et al., 2006; Zheng et al., 2021). In 2DSOIL, Eq. (1) is decoupled into three steps, which are liquid water transfer, heat transfer, and vapor flux (Wang et al., 2022a). Solving water and heat transfer one-by-one in a discrete time step provides two advantages: (a) to avoid solving high dimensional linear systems generated from the numerical schemes; (b) to enable a design that assigns liquid water, heat, and vapor transfers into three separate modules, which provides flexible programming architectures and adaptable controls for relatively complex Soil-Vegetation-Atmosphere-Transfer (SVAT) simulators (e.g., Timlin et al., 2019; Wang et al., 2020; Wang et al., 2021b; Wang et al., 2021c; Wang et al., 2022a). In this section, a partially coupled version of CHWT model used in 2DSOIL is considered as an example, and the MsFEM scheme proposed in Section 2 is generalized as a solver that can sequentially compute soil water content and soil temperature.

3.1. The partially coupled version of heat and water transfer model

Let Eq. (2) be the starting point. The partially coupled version of soil heat and water transfer in Wang et al. (2022a) is to rewrite Eq. (2) into the equations of the following three separate steps.

$$\begin{cases} \text{Step I (liquid water transfer)}: c_w\dfrac{\partial h}{\partial t} = \nabla\bullet\left[K(h,T)\nabla h\right] & (15a)\\ \text{Step II (heat transfer)}: c_h\dfrac{\partial T}{\partial t} = -\nabla\bullet\left[-\Lambda\nabla T + c_l\rho_l q_l(T-T_0)\right] & (15b)\\ \text{Step III (vapor transfer)}: \begin{cases} c_{\theta\theta}\dfrac{\partial h}{\partial t} + c_{\theta T}\dfrac{\partial T}{\partial t} = \nabla\bullet\left[d_{mv}(h,T)\nabla h + d_{tv}(h,T)\nabla T\right] & (15c)\\ c_{T\theta}\dfrac{\partial h}{\partial t} + c_{TT}\dfrac{\partial T}{\partial t} = -\nabla\bullet\left[L_0\rho_l q_v + c_v\rho_l q_v(T-T_0)\right] & (15d) \end{cases} \end{cases}$$

In Eq. (15), $c_w(\mathrm{cm}^{-1})$ represent the soil water capacity, and $c_h\left(\mathrm{J\,cm^{-3}\,K^{-1}}\right)$ is the soil volumetric heat capacity. For each discrete time step, the three steps are processed one-by-one. When solving liquid water transfer [Step I, Eq. (15a)], soil temperature is assumed to be unchanged with respect to time. When soil temperature is computed [Step II, Eq. (15b)], soil water content is supposed to be steady, and the liquid water flux q_l can be determined from Eq. (15a). Finally, in Eqs. (15c, d), both soil water potential and temperature are updated again based on the vapor flux, as well as the sensible and latent heat carried by the vapor flux. The "thermally driven liquid water flow $[D_{tl}(h,T)]$" is omitted in Eq. (15), because (a) $D_{tl}(h,T)$ is not included in the initial version of 2DSOIL (Timlin et al., 1996) and (b) the liquid water flow under temperature gradient contributes < 5% of the total liquid water flow (Prunty, 2009; Wang et al., 2022a), and it is often negligible in CHWT problems as reported by Lu et al. (2020).

Solving Steps I-III in Eq. (15) one-by-one in each discrete time step should provide results similar to the coupled version in Eq. (2). Compared to the fully coupled version [Eq. (2)], the interaction between water transfer and heat transfer is weakened in the partially coupled version, and it is only explicitly shown in the vapor transfer step [Eqs. (15c, d)]. However, interaction between water transfer and heat transfer can be included recursively through multiple time steps. A comprehensive comparison between the fully coupled version [Eq. (1)] and the partially coupled version [Eq. (15)] of soil heat and water transfer is shown in Wang et al. (2022a).

3.2. Establishment of a MsFEM sequential solver

For the partially coupled heat and water transfer, the MsFEM basis functions for soil water potential and soil temperature can be computed individually, following the leading differential terms in Eqs. (15a, b), respectively. Therefore, for a given coarse element M (Fig. 1), Eq. (10) can be converted as follows.

$$\begin{cases} \nabla \bullet \left[K_{sat}\nabla\varphi_h^{(M,i)}\right] = 0 \\ \nabla \bullet \left[\Lambda\nabla\varphi_T^{(M,i)}\right] = 0 \end{cases}, i = 1,2,3,4 \tag{16}$$

And the oscillatory boundary conditions for the MsFEM basis function along Edge I in coarse element M [see Fig. 1, lower diagram, and Eq. (11)] can also be simplified as.

$$\begin{cases} \dfrac{\partial}{\partial x}K_{sat}\dfrac{\partial}{\partial x}\varphi_h^{(M,1)} = 0 \\ \dfrac{\partial}{\partial x}\Lambda\dfrac{\partial}{\partial x}\varphi_T^{(M,1)} = 0 \end{cases} \tag{17}$$

Apparently, the connections between the two groups of basis functions $\mathscr{V}^h$ and $\mathscr{V}^T$ are neglected due to the elimination of $D_{tl}(h,T)$. However, the correlation between $\mathscr{V}^h$ and $\mathscr{V}^T$ always exists due to the interactions between soil water potential and soil temperature. The Petrov-Galerkin global formulation derived from Eq. (15) can be given as follows.

$$\begin{cases} \text{Step I}: \displaystyle\sum_{M\in C_{m\times m}}\sum_{i=1,2,3,4} c_w\frac{\partial h_{M,i}}{\partial t}\iint_\Omega \varphi_h^{(M,i)}\psi d\omega \\ \quad = -\displaystyle\sum_{M\in C_{m\times m}}\sum_{i=1,2,3,4} Kh_{M,i}\iint_\Omega \nabla\varphi_h^{(M,i)}\cdot\nabla\psi d\omega - \underbrace{\int_{\partial\Omega}\left(q_l^{Ext}+q_v^{Ext}\right)\psi dl}_{\text{external water or vapor fluxesas boundary conditions}}, \qquad \forall\psi\in\mathscr{V}^0, \quad (18a) \\ \text{Step II}: \displaystyle\sum_{M\in C_{m\times m}}\sum_{i=1,2,3,4} c_h\frac{\partial T_{M,i}}{\partial t}\iint_\Omega \varphi_T^{(M,i)}\psi d\omega \\ \quad = -\displaystyle\sum_{M\in C_{m\times m}}\sum_{i=1,2,3,4}\left[\Lambda h_{M,i}\iint_\Omega \nabla\varphi_T^{(M,i)}\cdot\nabla\psi d\omega\right] + \iint_\Omega\left[c_l\rho_l q_l\left(T_{up}-T_0\right)\right]\cdot\nabla\psi d\omega \\ \qquad - \underbrace{\int_{\partial\Omega} q_h^{Ext}\psi dl}_{\text{external conductive heat fluxes asboundary conditions}} - \underbrace{\int_{\partial\Omega}\left[c_l\rho_l q_l\left(T_{up}-T_0\right)+\left[L_0\rho_l q_v+c_v\rho_l q_v\left(T_{up}-T_0\right)\right]\right]\psi dl}_{\text{external sensible and latent heat fluxes as boundary conditions}}, \qquad \forall\psi\in\mathscr{V}^0, \quad (18b) \\ \text{Step III}: \begin{cases} \displaystyle\sum_{M\in C_{m\times m}}\sum_{i=1,2,3,4}\left[c_{\theta\theta}\frac{\partial h_{M,i}}{\partial t}\iint_\Omega \varphi_h^{(M,i)}\psi d\omega + c_{\theta\theta}\frac{\partial T_{M,i}}{\partial t}\iint_\Omega \varphi_T^{(M,i)}\psi d\omega\right] \\ \quad = -\displaystyle\sum_{M\in C_{m\times m}}\sum_{i=1,2,3,4}\left[d_{mv}h_{M,i}\iint_\Omega \nabla\varphi_h^{(M,i)}\cdot\nabla\psi d\omega + d_{tv}T_{M,i}\iint_\Omega \nabla\varphi_T^{(M,i)}\cdot\nabla\psi d\omega\right], \qquad \forall\psi\in\mathscr{V}^0, \quad (18c) \\ \displaystyle\sum_{M\in C_{m\times m}}\sum_{i=1,2,3,4}\left[c_{T\theta}\frac{\partial h_{M,i}}{\partial t}\iint_\Omega \varphi_h^{(M,i)}\psi d\omega + c_{TT}\frac{\partial T_{M,i}}{\partial t}\iint_\Omega \varphi_T^{(M,i)}\psi d\omega\right] \\ \quad = \displaystyle\iint_\Omega\left[L_0\rho_l q_v + c_v\rho_l q_v\left(T_{up}-T_0\right)\right]\cdot\nabla\psi d\omega, \qquad \forall\psi\in\mathscr{V}^0, \quad (18d) \end{cases} \end{cases}$$

In a given discretized time step, nodal values of soil water potential and temperature on the coarse grid can be obtained by solving Eq. (18) as the three proposed steps. The soil water potential and temperature values on the fine grid can be reconstructed using Eq. (14).

3.3. Illustrative Example

Example 2.5. **(*Application of the MsFEM Sequential Solver*).**

In this example, to demonstrate the MsFEM sequential solver presented in Section 3.2, we redo the simulation in Example 2.3 using three methods: the MsFEM scheme with $C_{20\times20}F_{5\times5}$ grid, the MsFEM sequential solver with $C_{20\times20}F_{5\times5}$ grid, and the standard FEM with $C_{20\times20}$ grid. Then, the solution error and the "sub-grid capturing error" of the three methods are computed relative to the standard FEM solution on the underlying grid $C_{100\times100}$. The evolution of errors with respect to time are presented in Fig. 5.

Due to the elimination of "thermally driven liquid water flow" and the decreasing of soil water and temperature interaction, the errors produced by MsFEM sequential solver slightly increase (about 5%) compared to the MsFEM scheme. However, the MsFEM scheme and the MsFEM sequential solver still outperform the standard FEM for both the soil water content and temperature solved on the coarse grid and the reconstructed values on the fine grid.

△.

4. Summary and future topics

The application of a multiscale finite element method (MsFEM) on coupled heat and water transfer (CHWT) problems is investigated in this study. Two groups of MsFEM basis functions are constructed to absorb the local variabilities of soil hydraulic and thermal conductivity, and a global formulation based on Petrov-Galerkin finite element method (FEM) is adopted to implement the proposed MsFEM scheme. Because partially coupled versions of heat and water transfer are used in existing soil simulators, such as Hydrus (Saito et al., 2006; Zheng et al., 2021) and 2DSOIL (Timlin et al., 1996; Wang et al., 2021c), the MsFEM scheme proposed in this study is exploited as a sequential solver to handle such variations. Since the MsFEM basis functions in this study can be determined in advance, using the MsFEM scheme does not essentially increase the computing load, and the illustration examples indicate that the MsFEM scheme can reduce the simulation errors by up-to 30% compared to the standard FEM, especially for the soil water content. Therefore, the MsFEM approach proposed in this study provides an effective numerical method for CHWT simulations in soils.

Spatial heterogeneities are only assumed in soil hydraulic and thermal conductivity in this study. Similar spatial variabilities may also occur for vapor transfer coefficients, such as d_{mv} or d_{tv}. Unfortunately, related soil studies are relatively rare. However, if those studies exist, the MsFEM scheme proposed in this study can be generalized by simply revising the construction of the MsFEM basis functions [Eq. (10) or (16)]. Furthermore, the MsFEM basis functions are pre-calculated in this study and not changed during time evolution. Thus, research on the adaptive updates of the basis functions can be a future development of the MsFEM scheme proposed in this study (e.g., Chung et al., 2015; Chung et al., 2016), which can be fulfilled either with the conventional partial differential equation solvers or with learning-based approaches.

CRediT authorship contribution statement

Chenyi Luo: Writing – original draft. **Yuanyuan Shi:** Writing – review & editing. **Dennis Timlin:** Methodology, Software, Writing – review & editing, Supervision. **Robert Ewing:** Writing – review & editing. **David Fleisher:** . **Robert Horton:** Writing – review & editing. **Katherine Tully:** Writing – review & editing. **Zhuangji Wang:** Conceptualization, Formal analysis, Methodology, Software, Writing – original draft, Writing – review & editing, Supervision.

Declaration of Competing Interest

The authors declare that they have no known competing financial interests or personal relationships that could have appeared to influence the work reported in this paper.

Acknowledgement

This study is based upon work supported by the Department of Agriculture, Agricultural Research Service under Agreement No. 58-8042-7-067; USDA National Institute of Food and Agriculture under Award No. 2018-68011-28372; USDA National Institute of Food and Agriculture under Award No. 2019-68012-29818; National Science Foundation under Grant 2037504; USDA-NIFA Multi-State Project 4188. The authors also received support from the University of Maryland, College Park, Iowa State University, and Beijing University of Chinese Medicine.

Declarations and Statements

1. The authors declare that they have no known competing financial interests or personal relationships that could have appeared to influence the work reported in this paper.

2. The numerical implementation of the model established in the paper, as well as supplementary materials for the examples, can be accessed in a GitHub repository at the link (https://github.com/cauwzj). Free access to the source code and supplementary materials is approved by all of the authors.

References

Aarnes, J.E., Efendiev, Y., Jiang, L., 2008. Mixed multiscale finite element methods using limited global information. SIAM Multiscale Model. Simul. 7, 655–676. https://doi.org/10.1137/070688481.

Arbogast, T., Boyd, K.J., 2006. Subgrid upscaling and mixed multiscale finite elements. SIAM J. Numer. Anal. 44, 1150–1171. https://doi.org/10.1137/050631811.

Babuska, I., Osborn, J.E., 1983. Generalized finite element methods: their performance and their relation to mixed methods. SIAM J. Numer. Anal. 20, 510–536. https://doi.org/10.1137/0720034.

Chen, F., Ren, L., 2008. Application of the finite difference heterogeneous multiscale method to the Richards' equation. Water Resour. Res. 44, W07413. https://doi.org/10.1029/2007WR006275.

Chung, E., Efendiev, Y., Leung, W.T., 2015. Residual-driven online generalized multiscale finite element methods. J. Comput. Phys. 302, 176–190. https://doi.org/10.1016/j.jcp.2015.07.068.

Chung, E., Efendiev, Y., Hou, T.Y., 2016. Adaptive multiscale model reduction with Generalized Multiscale Finite Element Methods. J. Comput. Phys. 320, 69–95. https://doi.org/10.1016/j.jcp.2016.04.054.

Dai, H., Zheng, Z., Ma, H., 2019. An explicit method for simulating non-Gaussian and non-stationary stochastic processes by Karhunen-Loève and polynomial chaos expansion. Mech. Syst. Signal Process. 115, 1–13. https://doi.org/10.1016/j.ymssp.2018.05.026.

Durlofsky, L.J., 1991. Numerical calculation of equivalent grid block permeability tensors for heterogeneous porous media. Water Resour. Res. 27, 699–708. https://doi.org/10.1029/91WR00107.

E, W., Ming, P., Zhang, P., 2005. Analysis of the heterogeneous multiscale method for elliptic homogenization problems. J. Amer. Math. Soc. 18 (1), 121–156.

Efendiev, Y., Ginting, V., Hou, T.Y., 2004. Multiscale finite element methods for nonlinear problems and their applications. Comm. Math. Sci. 2, 553–589.

Efendiev, Y., Hou, T.Y., 2009. Multiscale finite element methods, Surveys and Tutorials in the Applied Mathematical Sciences. Springer, New York.

Fish, J., Yuan, Z., 2007. Multiscale enrichment based on partition of unity for nonperiodic fields and nonlinear problems. Comput. Mech. 40, 249–259. https://doi.org/10.1007/s00466-006-0095-0.

Groenevelt, P.H., Kay, B.D., 1974. On the interaction of water and heat transport in frozen and unfrozen soils: II. The liquid phase. Soil Sci. Soc. Am. J. 38, 400–404. https://doi.org/10.2136/sssaj1974.03615995003800030012x.

He, X., Ren, L., 2005. Finite volume multiscale finite element method for solving the groundwater flow problems in heterogeneous porous media. Water Resour. Res. 41, W10417. https://doi.org/10.1029/2004WR003934.

He, X., Ren, L., 2006. A multiscale finite element linearization scheme for the unsaturated flow problems in heterogeneous porous media. Water Resour. Res. 42, W08417. https://doi.org/10.1029/2006WR004905.

He, X., Ren, L., 2009. An adaptive multiscale finite element method for unsaturated flow problems in heterogeneous porous media. J. Hydrol. 374, 56–70. https://doi.org/10.1016/j.jhydrol.2009.05.021.

Heitman, J.L., Horton, R., Ren, T., Ochsner, T.E., 2007. An Improved Approach for Measurement of Coupled Heat and Water Transfer in Soil Cells. Soil Sci. Soc. Am. J. 71, 872–880. https://doi.org/10.2136/sssaj2006.0327.

Heitman, J.L., Horton, R., Ren, T., Nassar, I.N., Davis, D.D., 2008. A Test of Coupled Soil Heat and Water Transfer Prediction under Transient Boundary Temperatures. Soil Sci. Soc. Am. J. 72, 1197–1207.

Hou, T.Y., Wu, X., 1997. A multiscale finite element method for elliptic problems in composite materials and porous media. J. Comput. Phys. 134, 169–189. https://doi.org/10.1006/jcph.1997.5682.
Hou, T.Y., Wu, X., Cai, Z., 1999. Convergence of multi-scale finite element method for elliptic problems with rapidly oscillating coefficients. Math. Comput. 68, 913–943. https://doi.org/10.1090/S0025-5718-99-01077-7.
Hou, T.Y., Wu, X., Zhang, Y., 2004. Removing the cell resonance error in the multiscale finite element method via a Petrov-Galerkin formulation. Comm. Math. Sci. 2, 185–205.
Jin, Y., Li, X., Zhao, M., Liu, X., Li, H., 2017. A mathematical model of fluid flow in tight porous media based on fractal assumptions. Int. J. Heat Mass Transf. 108, 1078–1088. https://doi.org/10.1016/j.ijheatmasstransfer.2016.12.096.
Juanes, R., Patzek, T.W., 2010. Multiscale-stabilized finite element methods for miscible and immiscible flow in porous media. J. Hydraul. Res. 42, 131–140. https://doi.org/10.1080/00221680409500056.
Li, C.F., Feng, Y.T., Owen, D.R.J., Davies, I.M., 2006. Fourier representation of random media fields in stochastic finite element modelling. Eng. Comput. 23, 794–817. https://doi.org/10.1108/02644400610689901.
Li, S., Wang, C., Shi, L., Yin, N., 2019. Statistical characteristics of the thermal conductivity of frozen clay at different water contents. Results Phys. 13, 102179 https://doi.org/10.1016/j.rinp.2019.102179.
Li, S., Luo, C., Yang, Y.i., Yang, L., Wu, L., Huang, T., Wang, Z., Anastasiou, E.K., 2021. Effects of biostabilization on engineering properties of geomaterials. Adv. Civ. Eng. 2021, 1–9.
Li, N., Yue, X., Ren, L., 2016. Numerical homogenization of the Richards equation for unsaturated water flow through heterogeneous soils. Water Resour. Res. 52, 8500–8525. https://doi.org/10.1002/2015WR018508.
Lu, Y., Lu, S., Horton, R., Ren, T., 2014. An empirical model for estimating soil thermal conductivity from texture, water content, and bulk density. Soil Sci. Soc. Am. J. 78, 1859–1868. https://doi.org/10.2136/sssaj2014.05.0218.
Lu, S., Ren, T., Horton, R., 2020. Estimating the components of apparent thermal conductivity of soils at various water contents and temperatures. Geoderma. 376, 114530 https://doi.org/10.1016/j.geoderma.2020.114530.
Milly, P.C.D., 1982. Moisture and heat transport in hysteretic, inhomogeneous porous media: A matric head-based formulation and a numerical model, Water Resour. Res. 18, 489–498. https://doi.org/10.1029/WR018i003p00489.
Philip, R., de Vries, D.A., 1957. Moisture movement in porous materials under temperature gradients. Trans. Am. Geophys. Union. 38, 222–232. https://doi.org/10.1029/TR038i002p00222.
Nassar, I.N., Horton, R., 1989. Water Transport in Unsaturated Nonisothermal Salty Soil: II. Theoretical Development. Soil Sci. Soc. Am. J. 53, 1330–1337. https://doi.org/10.2136/sssaj1989.03615995005300050005x.
Nassar, I.N., Horton, R., 1997. Heat, Water, and Solution Transfer in Unsaturated Porous Media: I - Theory Development and Transport Coefficient Evaluation. Trans. Porous Media 27, 17–38. https://doi.org/10.1023/A:1006583918576.
Phoon, K.K., Huang, S.P., Quek, S.T., 2002. Simulation of second-order processes using Karhunen-Loeve expansion. Comput. Struct. 80, 1049–1060. https://doi.org/10.1016/S0045-7949(02)00064-0.
Phoon, K.K., Huang, H.W., Quek, S.T., 2005. Simulation of strongly non-Gaussian processes using Karhunen-Loeve expansion. Probabilistic Eng. Mech. 20, 188–198. https://doi.org/10.1016/j.probengmech.2005.05.007.
Prunty, L., 2009. Soil water thermal liquid diffusivity. Soil Sci. Soc. Am. J. 73, 704–706. https://doi.org/10.2136/sssaj2008.0097.
Reddy, J.N. 2006. An introduction to the finite element method (3rd Ed.). McGraw-Hill Mechanical Engineering. McGraw-Hill Education: New York, Chicago, San Francisco, Athens, London, Madrid, Mexico City, Milan, New Delhi, Singapore, Sydney, Toronto.
Rienzner, M., Gandolfi, C., 2014. Investigation of spatial and temporal variability of saturated soil hydraulic conductivity at the field-scale. Soil Tillage Res. 135, 28–40. https://doi.org/10.1016/j.still.2013.08.012.
Saito, H., Simunek, J., Mohanty, B.P., 2006. Numerical analysis of coupled water, vapor, and heat transport in the vadose zone. Vadose Zone J. 5, 784–800. https://doi.org/10.2136/vzj2006.0007.
Scanlon, B.R., Milly, P.C.D., 1994. Water and heat fluxes in desert soils: 2. Numerical simulations. Water Resour. Res. 30, 721–733. https://doi.org/10.1029/93WR03252.
Shangguan, W., Dai, Y., Duan, Q., Liu, B., Yuan, H., 2014. A global soil data set for earth system modelling. J. Adv. Model. Earth Syst. 6, 249–263. https://doi.org/10.1002/2013MS000293.
Shen, J., Zhang, X., Liu, W., Zhang, Y., 2019. Fractal study in soil spatial variability and thermal conductivity. Therm. Sci. 23, 2849–2865. https://doi.org/10.2298/TSCI190109199S.
Simunek, J., Vogel, T. and van Genuchten, M., 1992. The SWMS 2D code for simulating water flow and solute transport in two-dimensional variably saturated media. Version 1.1. Research Report No. 126. US Salinity Lab.
Slodicka, M., 2002. A robust and efficient linearization scheme for doubly nonlinear and degenerate parabolic problems arising in flow in porous media. SIAM J. Sci. Comput. 23, 1593–1614. https://doi.org/10.1137/S1064827500381860.
Spiridonov, D., Vasilyeva, M., Chung, E.T., 2020. Generalized multiscale finite element method for multicontinua unsaturated flow problems in fractured porous media. J. Comput. Appl. Math. 370, 112594 https://doi.org/10.1016/j.cam.2019.112594.
Timlin, D., Pachepsky, Y.A., Acock, B., 1996. A design for a modular, generic soil simulator to interface with plant models. Agron. J. 88, 162–169. https://doi.org/10.2134/agronj1996.00021962008800020008x.
Timlin, D., Kim, S.H., Fleisher, D., Wang, Z., Reddy, V.R., 2019. Maize water use and yield in the solar corridor system: A simulation study. In: Deichman, C.L., Kremer, R. J. (Eds.), The solar corridor crop system: implementation and impacts. Elsevier Science, pp. 57–78. https://doi.org/10.1016/B978-0-12-814792-4.00003-6.
Wang, Z., Ankeny, M., Horton, R., 2017b. The impact of water vapor diodes on soil water redistribution. J. Hydrol. 552, 600–608. https://doi.org/10.1016/j.jhydrol.2017.07.009.
Wang, Z., Timlin, D., Gang, L., Fleisher, D., Sun, W., Beegum, S., Heitman, J., Ren, T., Chen, Y., Reddy, V.R., Tully, K., Horton, R., 2022b. Coupled heat and water transfer in heterogeneous and non-rigid soils: simulation using mixed finite element method. (in press).
Wang, Z., Schwartz, R., Kojima, Y., Chen, Y., Horton, R., 2017a. A Comparison of Second-Order Derivative Based Models for Time Domain Reflectometry Waveform Analysis. Vadose Zone Journal 16 (7), 1–10.
Wang, Z., Timlin, D., Kouznetsov, M., Fleisher, D., Li, S., Tully, K., Reddy, V.R., 2020. Coupled model of surface runoff and surface-subsurface water movement. Adv. Water Resour. 137, 103499 https://doi.org/10.1016/j.advwatres.2019.103499.
Wang, Z., Timlin, D., Kojima, Y., Luo, C., Chen, Y., Li, S., Fleisher, D., Tully, K., Reddy, V. R., Horton, R., 2021a. A piecewise analysis model for electrical conductivity calculation from time domain reflectometry waveforms. Comput. Electron. Agric. 182, 106012 https://doi.org/10.1016/j.compag.2021.106012.
Wang, Z., Timlin, D., Li, S., Fleisher, D., Dathe, A., Luo, C., Dong, L., Reddy, V.R., Tully, K., 2021b. A diffusive model of maize root growth in MAIZSIM and its applications in Ridge-Furrow Rainfall Harvesting. Agri. Water Manag. 254, 106966 https://doi.org/10.1016/j.agwat.2021.106966.
Wang, Z., Thapa, R., Timlin, D., Li, S., Sun, W., Beegum, S., Fleisher, D., Mirsky, S., Cabrera, M., Sauer, T., Reddy, V.R., Horton, R., Tully, K., 2021c. Simulations of water and thermal dynamics for soil surfaces with residue mulch and surface runoff. Water Resour. Res. 57 https://doi.org/10.1029/2021WR030431.
Wang, Z., Timlin, D., Fleisher, D., Sun, W., Beegum, S., Li, S., Chen, Y., Reddy, V.R., Tully, K., Horton, R., 2022a. Modelling vapor transfer in soil water and heat simulations: a modularized, partially-coupled approach. J. Hydrol. 608, 127541 https://doi.org/10.1016/j.jhydrol.2022.127541.
Zeng, Y., Su, Z., Wan, L., Wen, J., 2011a. A simulation analysis of the advective effect on evaporation using a two-phase heat and mass flow model. Water Resour. Res. 47, W10529. https://doi.org/10.1029/2011WR010701.
Zeng, Y., Su, Z., Wan, L., Wen, J., 2011b. Numerical analysis of air-water-heat flow in unsaturated soil: Is it necessary to consider airflow in land surface models? J. Geophys. Res. 116, D20107. https://doi.org/10.1029/2011JD015835.
Zheng, C., Simunek, J., Zhao, Y., Lu, Y., Liu, X., Shi, C., Li, H., Yu, L., Zeng, Y., Su, Z., 2021. Development of the Hydrus-1D freezing module and its application in simulating the coupled movement of water, vapor, and heat. J. Hydrol. 598, 126250 https://doi.org/10.1016/j.jhydrol.2021.126250.